Systematic study of the α-optical potential via elastic scattering near the $Z = 50$ region for p-process nuclei

A. Palumbo,[*] W. P. Tan,[†] J. Görres, A. Best, M. Couder, R. Crowter,[‡] R. J. deBoer, S. Falahat,[§] P. J. LeBlanc,[‖] H. Y. Lee,[¶] S. O'Brien,[**] E. Strandberg,[††] and M. Wiescher
Department of Physics, University of Notre Dame, Notre Dame, Indiana 46556, USA

J. P. Greene
Physics Division, Argonne National Laboratory, 9700 S. Cass Avenue, Argonne, Illinois 60439, USA

Zs. Fülöp, G. G. Kiss, and E. Somorjai
Institute of Nuclear Research (ATOMKI), P.O. Box 51, H-4001 Debrecen, Hungary

N. Özkan, G. Efe, and R. T. Güray
Kocaeli University, Department of Physics, Umuttepe 41380, Kocaeli, Turkey
(Received 16 December 2011; revised manuscript received 29 February 2012; published 29 March 2012)

Production of proton-rich nuclei beyond iron in stars proceeds via the p process, i.e., a sequence of photodisintegration reactions, (γ,n), (γ,p), and (γ,α) on heavy nuclei at temperatures of 2–3 $\times$ 10^9 K. The involved reaction rates are typically calculated with the statistical Hauser-Feshbach (HF) model. However, the HF model performs poorly in calculating the critical (γ,α) rates due to the uncertainty of the alpha optical potentials applied. To test the reliability of the HF calculations and provide a systematic understanding of the α optical potential at energies of astrophysical interest, a series of precision α scattering measurements were carried out at the Notre Dame FN Tandem Accelerator. Specifically, ^{106}Cd, ^{118}Sn, and ^{120,124,126,128,130}Te were studied at energies both below and above the Coulomb barrier. A new parametrization of the α optical potential was derived of the elastic scattering cross section data. The derived potential was applied for calculating the α-induced reaction cross sections on these nuclei using the HF approach. The results were compared to the corresponding experimental values obtained from previous activation measurements on Cd, Sn, and Te isotopes.

DOI: 10.1103/PhysRevC.85.035808 PACS number(s): 24.10.Ht, 26.30.−k, 25.55.Ci

I. INTRODUCTION

The majority of the heavy elements beyond iron are produced via neutron capture processes in stars, the so-called s and r processes. However the 35 stable nuclei on the proton-rich side of the valley of stability, known as the p nuclei, are shielded from these processes and have to be synthesized via the so-called p process [1]. These p nuclei in the mass range from ^{74}Se to ^{196}Hg are produced as the p process proceeds via a sequence of photodisintegration reactions: (γ,n), (γ,p), and (γ,α) starting on the heavy seed nuclei produced in previous nucleosynthesis from neutron-capture processes. The required high temperature (2–3 $\times$ 10^9 K) and high photon-flux conditions can exist in astrophysical sites like supernova explosions [2–5].

Complete network calculations for the p nuclei abundances involve more than 20 000 nuclear reactions of almost 2000 nuclei. These reaction rates are typically calculated with the statistical Hauser Feshbach (HF) model [6]. In particular, the (γ,α) rates are critical for the production of heavy p nuclei and the branchings of the p process path [7]. However, the HF model performs poorly in calculating these rates due to the uncertainty of the model parameters applied. To improve the reliability of the HF reaction rates, experimental verifications and constraints on these model parameters are needed.

Direct measurements of the (γ,α) rates are scarce due to the difficulty of γ beam experiments [8]. On the other hand, a direct measurement alone can not provide the rate as only the ground state of the target is involved. Contributions from the excited states thermally populated in hot stellar environments have to be calculated. Contrarily and complementarily, the inverse (α,γ) reactions have often been studied via activation technique. In recent years, a number of α-beam activation measurements have been conducted for targets relevant to p process [9–17]. Cross sections of the corresponding (α,x) reactions were measured at or close to the astrophysically relevant energy.

[*]Present address: Brookhaven National Laboratory, Upton, NY 11973.
[†]wtan@nd.edu
[‡]Present address: University of Surrey, Surrey, UK.
[§]Present address: Institute for Environmental Research, Australian Nuclear Science and Technology Organization, Kirrawee DC, Australia.
[‖]Present address: CANBERRA Industries, Inc., Meriden, CT 06450.
[¶]Present address: LANSCE-NS, Los Alamos National Laboratory, NM 87545.
[**]Present address: US Government, 13th St. NW, Washington DC 20009.
[††]Present address: Lockheed Martin Aeronautics Company, Palmdale, CA 93599.

Calculations using the HF approach have been compared to the measured (α,γ) cross sections. Generally large discrepancies, within a factor of 10, were observed between the data and model predictions. In particular, the widely used NON-SMOKER calculations [18] tend to overpredict the (α,γ) cross sections especially at lower energies [12,13]. One of the possible causes is the uncertainty of the α-optical potential used in the HF calculations. Different global or regional α-optical potential models can change the predictions by almost an order of magnitude [13]. These α potential models were often parametrized by fitting the differential cross sections of elastic scattering at relatively high energies. In order to determine better local α-optical potentials for calculating the (α,γ) cross sections, α-elastic scattering experiments have been performed at lower and more relevant energies on p-process-related targets [19–24].

The variation of the α-elastic scattering cross sections along an isotopic chain was studied by Galaviz *et al.* with ^{112,124}Sn targets [21]. More recently, such variations along the Cd isotopic and $N = 62$ isotonic chains were investigated by Kiss *et al.* [24] by combining their new data on ^{110,116}Cd with previous data on ^{106}Cd and ^{112}Sn. These studies are important for understanding the evolution of the α optical potential along the isotopic and isotonic chains, which can be used for the HF calculations on exotic nuclei where experiments are not feasible in the foreseeable future.

However, the previous elastic scattering studies are still limited in the isotopic and energy ranges. Only two or at most three isotopes were measured along a chain. Detailed differential cross sections were measured at beam energies below 20 MeV where ambiguities of the potential parameters are difficult to solve. For the purpose of parametrizing the α-optical potential for the HF calculations, systematic studies of the extended energy and isotopic dependence of the α-optical potential parametrization are still lacking.

To test the reliability of the HF calculations and provide a systematic understanding of the α-optical potential at energies of astrophysical interest, a series of precision α scattering measurements were carried out at the University of Notre Dame. Specifically, ^{106}Cd, ^{118}Sn, and ^{120,124,126,128,130}Te were studied at energies both below and above the Coulomb barrier: 17, 19, 22, 24.5, and 27 MeV. The extended energy range helps probe the energy dependence of the potential parameters and guide the extrapolation down to the astrophysical energy range. The systematic study of almost all stable Te isotopes helps determine the isotopic dependence of the potential and therefore extend the application to the unstable p-rich nuclei away from the stability valley. Additional measurements with ^{106}Cd and ^{118}Sn provide a test on the charge dependence. A new parametrization of the α-optical potential derived from the elastic scattering data was used for calculating the cross sections of α induced reactions. Previous activation measurements on Te, Cd, and Sn isotopes are reviewed and compared to the calculations using the new parametrization.

II. EXPERIMENTAL DETAILS

A ^{4}He beam from 17 MeV up to 27 MeV was produced at the Notre Dame FN Tandem Accelerator and bombarded on Cd, Sn, and Te targets. An array of 32 silicon photodiode detectors were constructed to measure the angular distribution of scattered alpha particles. The array was mounted inside a scattering chamber of 1.6 m in diameter [25] as shown in Figs. 1 and 2. Two of the detectors were fixed at a distance of 65.30 cm from the target and placed at 15° on either side to monitor the beam and the target. Thirty of them were mounted on a rotatable table with angular position reproducible to an accuracy of 0.01°. The detectors on the table were 2.5° in angular separation covering a total angular range of 72.5°. As illustrated in Fig. 1, the table was rotated during the experiments to three positions for three different angular coverages: 22.5°–95° for position F1, 32.5°–105° for position F2, and 95°–167.5° for position B. The detectors were placed at a distance of 64.26 cm from the target with a small collimator in front of each. This resulted in a solid angle coverage of about 8.7×10^{-5} sr for each detector.

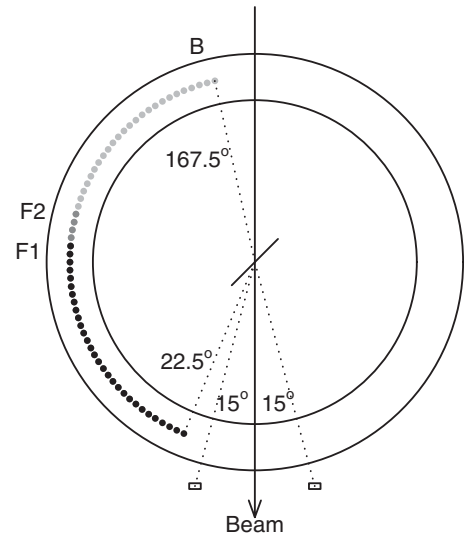

FIG. 1. Schematic setup of this experiment. The two monitor detectors were fixed at 15°. The array of 30 silicon detectors (small black and grey circles) were mounted on a rotatable table to cover an angular range of 22.5° to 167.5° in 2.5° increments. The three different table positions are labeled F1, F2, and B for the three angular coverages of the array, respectively.

For high precision scattering cross section measurements, two different approaches were used to precisely determine the solid angle coverage of each detector. In the off-line approach, the solid angle of each detector was measured separately prior

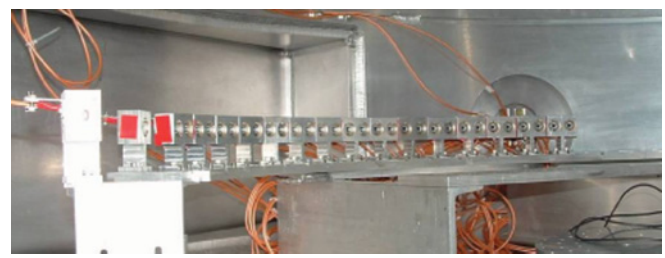

FIG. 2. (Color online) Photograph of the silicon photodiode detector array inside the scattering chamber.

TABLE I. Properties of the targets used in the experiment.

target	enrichment	thickness [μg/cm^2]
$^{120}TeO_2$	99.4%	130–210
$^{124}TeO_2$	99.5%	190–230
^{126}Te	99.0%	140
$^{128}TeO_2$	98.8%	180–210
^{130}Te	99.8%	120–160
$^{118}SnO_2$	97.0%	250–280
^{106}Cd	86.4%	300

to the experiment using a calibrated α source at a fixed position. After the beam runs, the same α source was placed at the target position to simultaneously measure the solid angles of all the detectors in the same positions as they were during the beam time. The two independent approaches showed consistent results for the solid angles. The measured solid angles were applied for calculating the cross sections in order to accurately compensate for the variations (up to 2%) in collimator diameter from machining error. The uncertainty from the detector solid angles was determined to be 1% after the corrections.

To obtain high precision isotopic cross sections, highly enriched isotopes were used for making thin targets (listed in Table I). The impurities of the targets have negligible effect on the measured cross sections as discussed in the next section. Self-supported tellurium foils are difficult to make and easy to destroy when exposed to particle beams due to the low melting point of tellurium metal [26]. All of the tellurium targets were evaporated onto 20 μg/cm^2 thick carbon foils at Argonne National Laboratory [27] and the Sn targets were prepared similarly at Notre Dame. The Cd targets were obtained commercially from Micromatter [28]. For the metallic targets, alpha beam currents up to 120 enA were employed. The oxide targets showed a higher stability in beam with no sign of degradation for twice as much beam intensity. As shown in the next section, the oxygen content in the target and carbon backings did not adversely interfere with the measurement.

III. DATA ANALYSIS

Figure 3 shows the energy spectra of scattered alpha particles on ^{120}Te target at angles of 25° and 165° and energies of 17 and 27 MeV, respectively. The rightmost peaks labeled as "g.s." in the plots are from the elastic scattering. The peaks from inelastic scattering of ^{120}Te at the 560 keV and 1103 keV levels are also shown as well as the ones from carbon and oxygen isotopes. The elastic peaks of the heavy elements are well separated from the inelastic ones and others from light elements like C and O in the target. The continuum background observed in more forward angles (bottom panels) comes from the multiscattering events. However, its effect is negligible as it is more than three orders of magnitude lower than the elastic peaks of interest.

To avoid the difficulty of measuring directly the target thickness and the beam current to high precision we normalized the measured cross sections to Rutherford. The

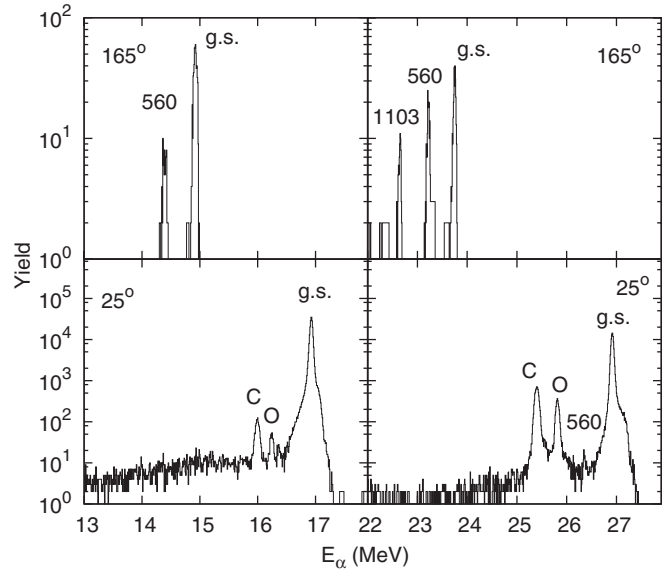

FIG. 3. Scattered α energy spectra on ^{120}Te target at angles of 25° (bottom) and 165° (top). Spectra for two different beam energies of 17 (left) and 27 (right) MeV are shown.

Rutherford cross section at small forward angles is a very good approximation for elastic scattering. The two monitor detectors at 15° therefore provided the in-beam normalization for obtaining the differential elastic cross sections from the other detectors [19–24].

The differential elastic cross sections for Te, Sn, and Cd targets are normalized as ratios to the Rutherford cross sections as shown in Figs. 4–10 where the error bars represent the combined statistical and systematic errors discussed above. The effect of the target impurities can be estimated from the difference between the cross sections of neighboring Te isotopes, which is about <5% in forward angles and <20% in

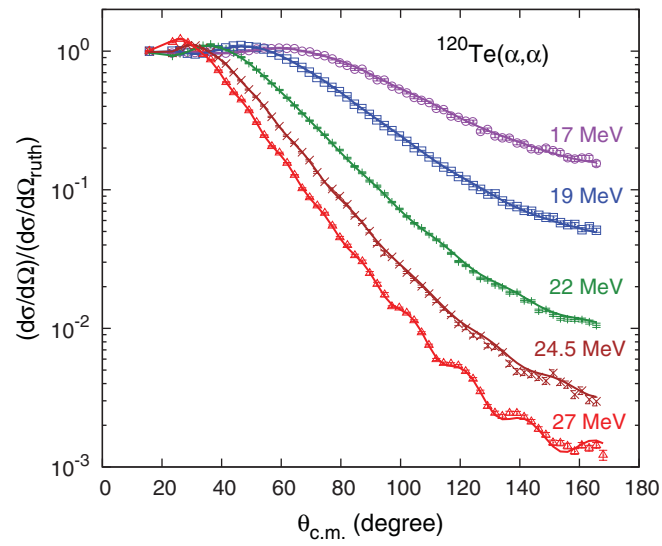

FIG. 4. (Color online) Normalized α elastic scattering cross sections on ^{120}Te target. The solid lines are the calculations using the new α potential parametrization described in Sec. IV B.

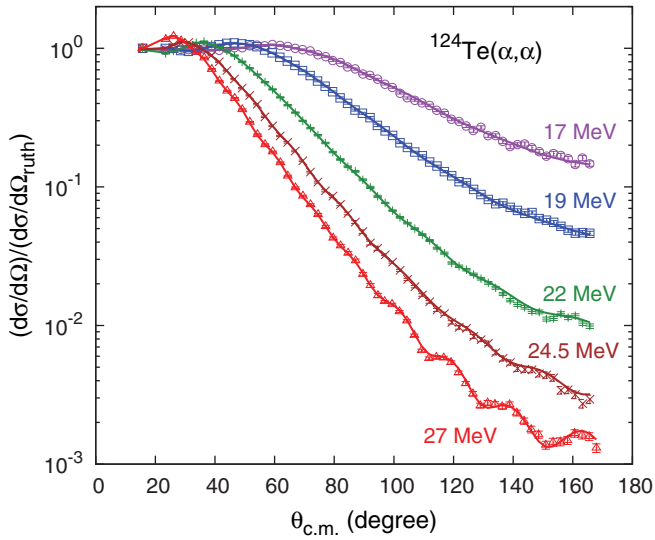

FIG. 5. (Color online) Normalized α elastic scattering cross sections on ^{124}Te target. The solid lines are the calculations using the new α potential parametrization described in Sec. IV B.

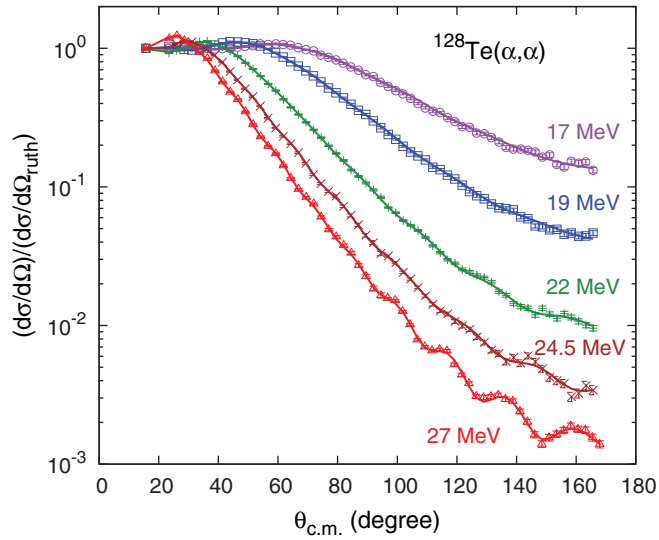

FIG. 7. (Color online) Normalized α elastic scattering cross sections on ^{128}Te target. The solid lines are the calculations using the new α potential parametrization described in Sec. IV B.

backward angles. A typical 1% impurity in Te targets can cause an error of much less 1% in measurement of cross sections. Therefore, the uncertainty of the cross sections for Te and Sn targets at forward angles is dominated by ∼1% systematic error while, at backward angles, by statistical error of about 4–8%. For the worst case of ^{106}Cd (86.4% enrichment), previous measurements on more enriched Cd targets (96.5% enrichment) in limited energy range of 16.1–19.6 MeV [22,24] as shown in Fig. 11 were compared and the impurities of our targets were estimated to cause an error of <2% on cross sections in forward angles and <10% in backward angles.

IV. α-OPTICAL POTENTIALS

A. Global optical potential models

Many global or regional α-optical potential models have been proposed in the past few decades. Due to the spinless nature of alpha particles, simple Woods-Saxon form factors were widely used in both real and imaginary parts of the nuclear potential in these models. Some of these models have been applied in the network calculations for the nucleosynthetic processes, in particular, for the p process. However, comparisons with simple elastic data at low energy are needed for these models before we can justify their predictions of the α-induced reaction rates. Figure 12 shows such an example for ^{120}Te(α,α) at 27 MeV. The experimental

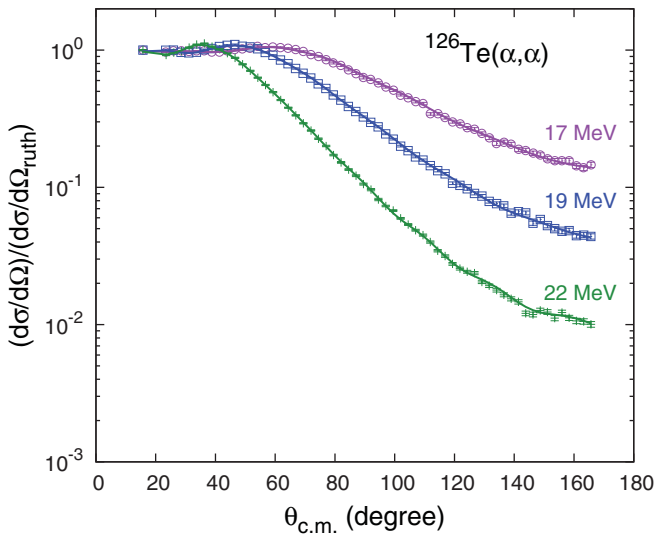

FIG. 6. (Color online) Normalized α elastic scattering cross sections on ^{126}Te target. The solid lines are the calculations using the new α potential parametrization described in Sec. IV B.

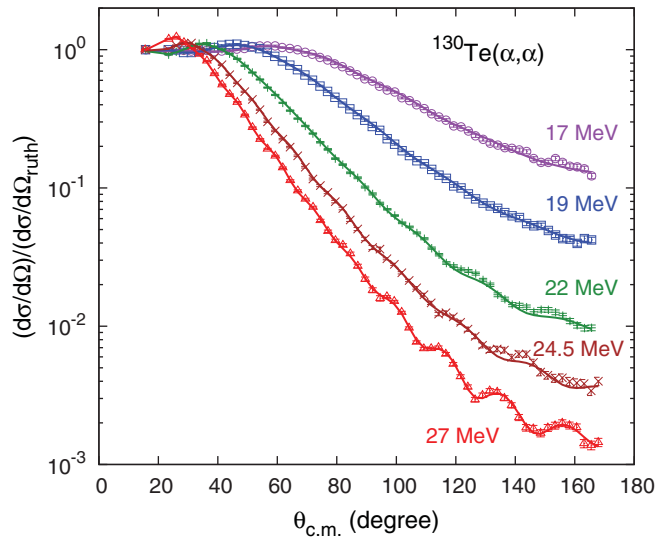

FIG. 8. (Color online) Normalized α elastic scattering cross sections on ^{130}Te target. The solid lines are the calculations using the new α potential parametrization described in Sec. IV B.

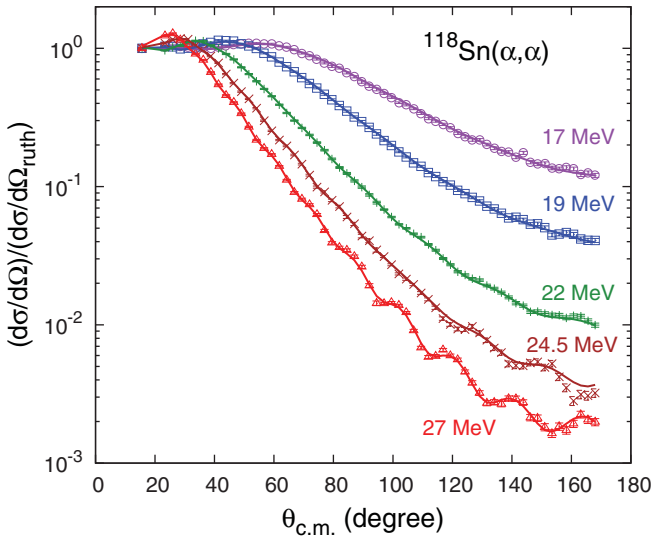

FIG. 9. (Color online) Normalized α elastic scattering cross sections on ^{118}Sn target. The solid lines are the calculations using the new α potential parametrization described in Sec. IV B.

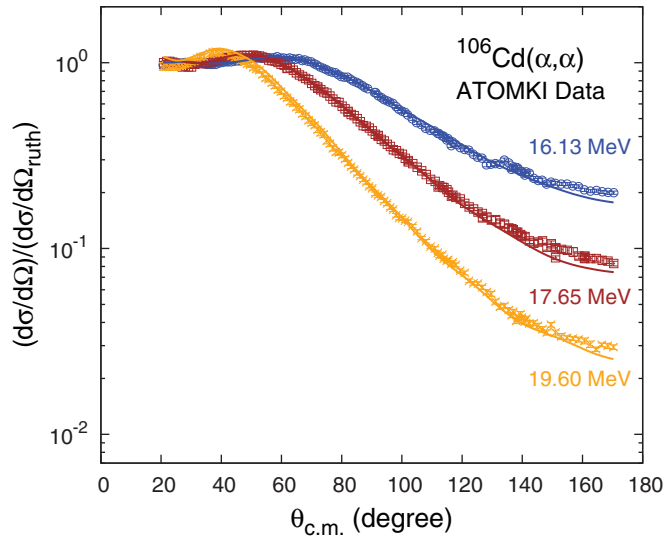

FIG. 11. (Color online) Normalized α elastic scattering cross sections on ^{106}Cd target from previous ATOMKI data [22,24]. The solid lines are the calculations using the new α potential parametrization described in Sec. IV B.

differential cross sections from this work are compared to the calculations of the four widely used global or regional models by McFadden and Satchler [29], Avrigeanu *et al*. [30], Fröhlich and Rauscher [31–33], and Demetriou *et al*. (Potential I) [34], respectively. Significant discrepancies between the data and the models are observed. In particular, the model of Avrigeanu *et al*. dramatically over-predicts the diffraction oscillations. The model of Demetriou *et al*. (Potential I) has better overall agreement with the data, but it under-predicts the oscillations. The other two models systematically overpredict the cross sections at large angles. Such discrepancies have been observed for all the other target and energy combinations investigated in this study.

To further test the isotopic dependence, the ratio of the normalized cross section of ^{130}Te to that of ^{120}Te at 27 MeV is plotted in Fig. 13 in a similar way to the previous work [21,24]. The experimental data are compared to the predictions from the four global or regional models as well. None of the models can reproduce the data well. In particular, the systematic overprediction of the ratio in the model of Demetriou *et al*. (Potential I) results from its much worse prediction of the cross sections on ^{130}Te than that on ^{120}Te. In the next section, a new parametrization is developed from the new data set in order to more reliably calculate the corresponding (α,x) rates.

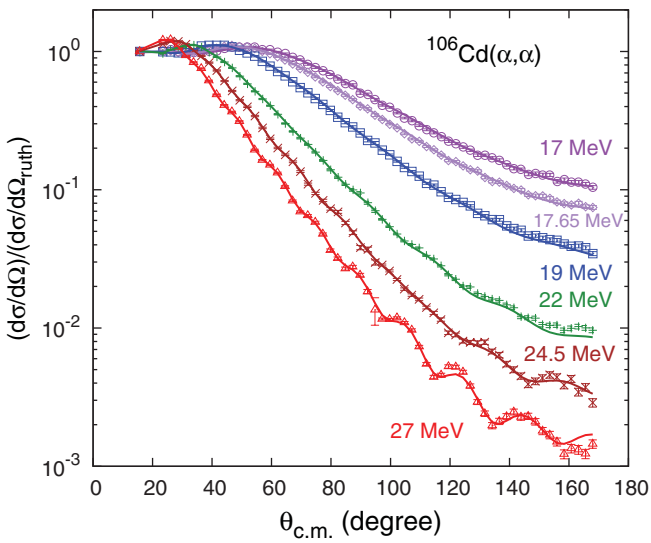

FIG. 10. (Color online) Normalized α elastic scattering cross sections on ^{106}Cd target. The solid lines are the calculations using the new α potential parametrization described in Sec. IV B.

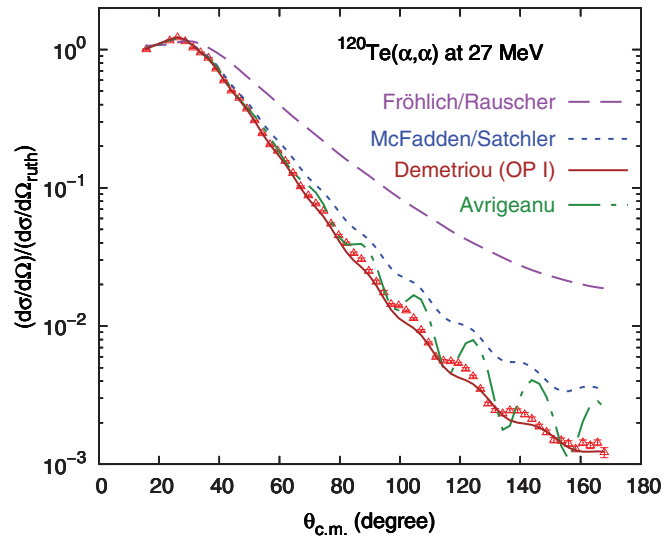

FIG. 12. (Color online) Normalized α elastic scattering cross sections on ^{120}Te target at 27 MeV are compared to the predictions from various global or regional optical potential models. See text for details.

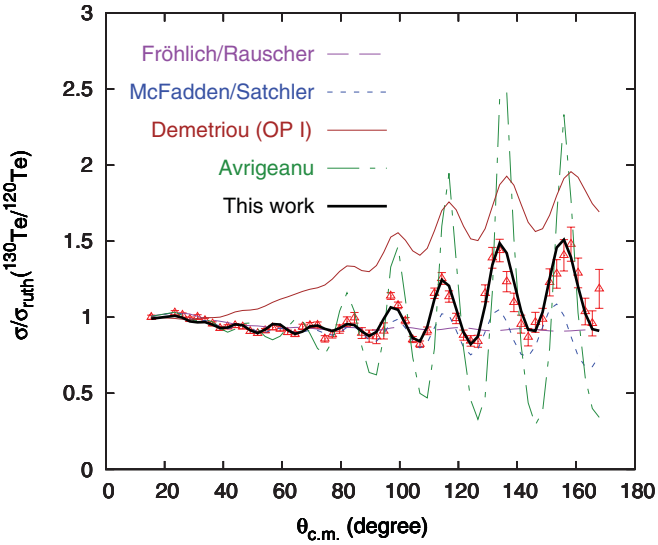

FIG. 13. (Color online) The ratio of normalized α elastic cross section on ^{130}Te to that on ^{120}Te at 27 MeV is plotted and compared to the calculations from this work and various global or regional optical potential models. See text for details.

B. New parametrization

In light of the failure of the global models in describing the elastic data, there has been great effort in recent years for developing local α optical potentials for specific nuclei [19–24]. However, these local potentials are limited in both energy and isotopic ranges and therefore difficult to parametrize. In this section, we introduce a new parametrization with both mass and energy dependences for the α optical potential from our new elastic data in order to apply it to the HF calculations in the next section. Note that the new parametrization has features similar to the global potentials of Demetriou *et al.* [34] which also aimed at the p-process studies.

For a spherical nucleus, the α-optical potential, as the spin-orbit interaction vanishes, can be written as

$$V(r) = V_c(r) + V_n(r) + i(V_v(r) + V_s(r)), \tag{1}$$

where the Coulomb potential V_c is obtained assuming a uniform charge distribution with a radius R_c and the imaginary terms of the nuclear potential V_v and V_s for volume and surface contributions, respectively, are chosen in Woods-Saxon form,

$$\begin{aligned} V_v(r) &= W_v \Big/ \left(1 + \exp\left(\frac{r - R_v}{a_v}\right)\right), \\ V_s(r) &= W_s \exp\left(\frac{r - R_s}{a_s}\right) \Big/ \left(1 + \exp\left(\frac{r - R_s}{a_s}\right)\right)^2. \end{aligned} \tag{2}$$

The real term of the nuclear potential V_n is parametrized from the double folding potential,

$$V_n(r) = \lambda V_f(r/\omega), \tag{3}$$

where the folding potential is calculated using the effective NN interaction of the density dependent M3Y form [35,36] with the energy dependence of the parameters being adopted from Ref. [37].

TABLE II. Charge density parameters and radii used in the optical potential calculations.

target	c [fm]	t [fm]	R_c [fm]
^{120}Te	5.47106	2.4289	6.08012[a]
^{124}Te	5.53197	2.340	6.09364[b]
^{126}Te	5.56385	2.295	6.10225[b]
^{128}Te	5.59334	2.253	6.11054[b]
^{130}Te	5.62203	2.209	6.11771[b]
^{118}Sn	5.442	2.386	6.03369[c]
^{106}Cd	5.2875	2.30	5.85373[d]

[a]extrapolated from Ref. [39] assuming a linear dependence on $A^{1/3}$.
[b]From Ref. [39].
[c]From Ref. [38].
[d]From Ref. [40].

To calculate the double folding potential, the sum-of-Gaussians parametrization is used for the charge density distribution of α particles [38]. The charge density distributions of the target nuclei are approximated by the two-parameter Fermi distribution, $1/(1 + \exp(4 \ln 3(r - c)/t))$ where the parameters are taken or extrapolated from experimental values [38–40]. The radius R_c for the Coulomb potential is obtained using $R_c = \sqrt{5/3} R_{\rm rms}$ where the rms radius $R_{\rm rms}$ is calculated from the corresponding target density distribution. Table II shows the parameters used in the calculations.

The elastic scattering cross sections were calculated from the above optical potentials using the code A0 [41,42]. MINUIT [43], a numerical minimization package from CERN, was adapted in the code for the fitting and optimization of the parameters. To best fit all the data in this work, the following parametrization regarding the energy and mass dependences of the parameters in Eqs. (2) and (3) was introduced:

$$\begin{aligned} W_v &= (v_1 + 0.0267536A)E_\alpha + (v_2 - 0.000858191A)E_\alpha^2, \\ R_v &= 1.690A^{1/3}, \\ a_v &= 1.58109 - 0.23479A^{1/3}, \\ W_s &= -\frac{290.0}{1 + \exp(s_0 - 0.1A - E_\alpha)}, \\ R_s &= 1.270A^{1/3}, \\ a_s &= a_0 + 0.0570676A^{1/3}, \\ \lambda &= 1.98888 - 0.00678209A + 0.0052E_\alpha, \\ \omega &= \omega_0 + 0.171254A^{1/3} + 0.000836E_\alpha, \end{aligned} \tag{4}$$

where the units are in fm and MeV and the parameters v_1, v_2, s_0, a_0, and ω_0 are constants, listed in Table III, for Te, Sn, and Cd isotopes studied in this work. The energy dependence was derived from all the data sets on Te, Sn, and Cd while

TABLE III. The parameters used in the new parametrization from Eq. (4) for different targets of Te, Sn, and Cd.

target	v_1	v_2	s_0	a_0	ω_0
Te	−3.67306	0.110442	29.4	−0.104193	0.137581
Sn	−3.44339	0.102558	28.1	−0.094009	0.141724
Cd	−3.00841	0.0878395	25.9	−0.066380	0.166275

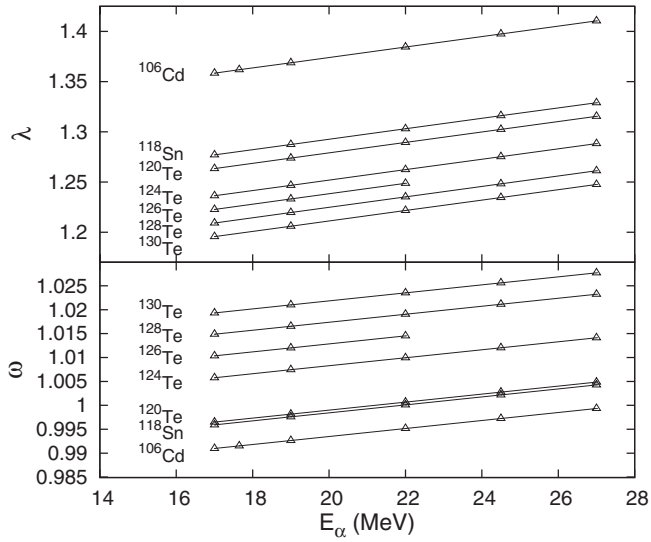

FIG. 14. The linear parametrization of λ and ω in Eq. (4) is plotted as function of α-beam energy for all the targets. The triangle symbols represent the energy points measured in this work.

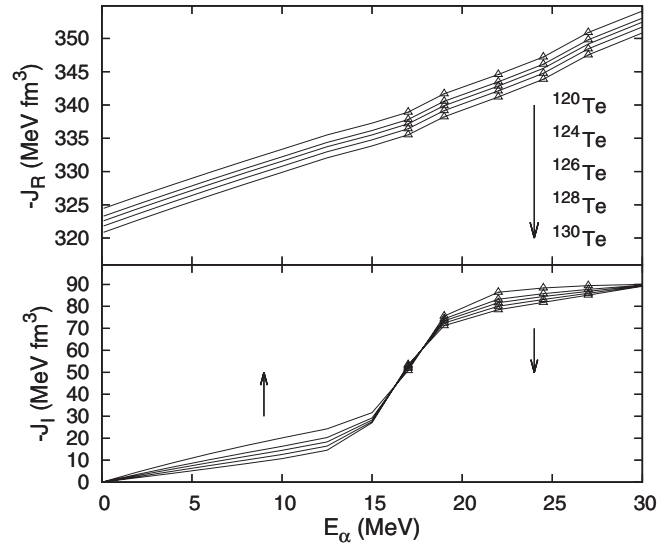

FIG. 15. The volume integrals of the real (top panel) and imaginary (bottom panel) nuclear potentials are plotted as function of α-beam energy for all Te targets. The arrows indicate the order of the curves with respect to different Te isotopes. Note that the order of the imaginary integral curves at $E_\alpha > 17$ MeV is the same as that for the real potential but reversed at $E_\alpha < 17$ MeV. The triangle symbols represent the energy points measured in this work.

the mass dependence was determined from the data on the Te isotopic chain. The same mass dependence was assumed for the Sn and Cd targets. So the parameters listed in Table III reflect the remaining dependence on the atomic number. A charge dependence was not formulated as the atomic number range of our targets ($Z = 48$–52) is very limited. Note that the numbers provided in Tables II and III and Eq. (4) contain many digits in order to accurately reproduce the potentials used in this work.

Figure 14 illustrates the energy dependence of the real nuclear potential parameters λ and ω for all the targets. As seen in the plot, ω values are very close to 1 within about 2% and λ values vary between 1.2 and 1.4, which are in agreement with previous studies on local optical potentials [19–24].

To demonstrate the energy dependence of the new parametrization and compare it with previous studies, we use the volume integrals of the nuclear potential per interacting nucleon pair J_R for the real part and J_I for the imaginary part, which are defined as follows:

$$J_R = \frac{1}{A_p A_t} \int V_n(r) d^3r, \tag{5}$$

$$J_I = \frac{1}{A_p A_t} \int (V_v(r) + V_s(r)) d^3r, \tag{6}$$

where A_p and A_t are the mass numbers for projectile and target, respectively. The volume integral of the real nuclear potential increases slightly as α-beam energy increases as shown in the top panel of Fig. 15 for all the Te targets. A similar trend in this energy range has also been observed in previous studies [19,20,44]. The behavior of the volume integral of the imaginary potential is shown in the bottom panel of Fig. 15. It stays relatively flat at energies well above the Coulomb barrier, then drops quickly when the energy falls just below the Coulomb barrier, and gradually vanishes when the energy decreases to zero. Note that the order of the volume integral curves is reversed when it crosses over the turning point at $E_\alpha = 17$ MeV. Similar energy dependence of the imaginary integral is also seen in previous studies [19,20,44]. However, the details of the low energy tail depend on the specific treatment of the parametrization. In our case, we applied a Fermi-type function for the surface parameter W_s in Eq. (4). Consequently, the surface term dominates the imaginary volume integral (about 60–70%) at $E_\alpha > 17$ MeV but drops quickly to zero when E_α is well below 17 MeV. Therefore, the low energy tail of the imaginary volume integral comes mostly from the slowly varying volume term.

Using the new parametrization proposed above, elastic scattering cross sections were calculated and compared to the experimental data as shown in Figs. 4–10. The new parametrization of the optical potential reproduced the data very well with a χ^2 per degree of freedom χ^2/F about 2 or less in most cases and $\chi^2/F = 4.2$ in the worst case for ^{106}Cd. This is much better than the global or regional models as demonstrated in Fig. 12. Previous data on ^{106}Cd [22,24] were also compared to the new parametrization predictions as shown in Fig. 11. The slight differences at backward angles may stem from the impurities of the Notre Dame ^{106}Cd targets which the new parametrization for ^{106}Cd is based upon. The ratio of the normalized cross section on ^{130}Te to that on ^{120}Te at 27 MeV was calculated with the new parametrization and shown in Fig. 13. It also reproduced the data very well, clearly better than the other models. The new parametrization was used for calculating the cross sections of the (α,x) reactions in the next section.

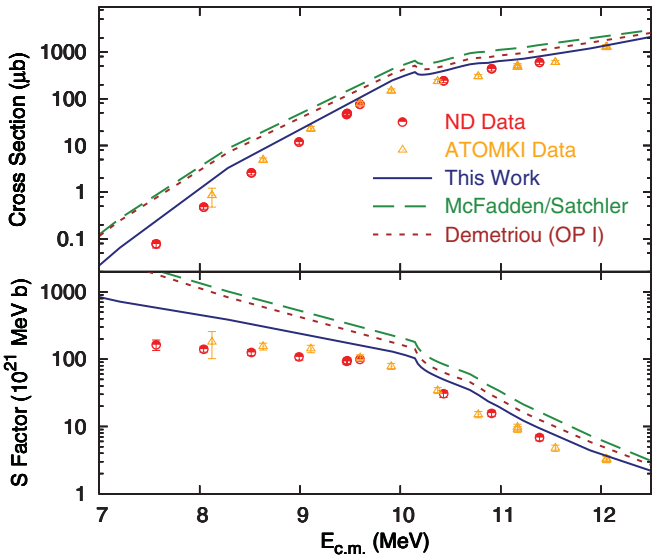

FIG. 16. (Color online) Cross sections and S factors of ^{106}Cd(α,γ). Experimental data points were taken from Ref. [12]. The solid line was calculated using the new parametrization for the α-optical potential while the calculations from the McFadden and Satchler potential [29] (dashed lines) and the potential of Demetriou *et al.* (Potential I) [34] (dotted lines) were also shown for comparisons.

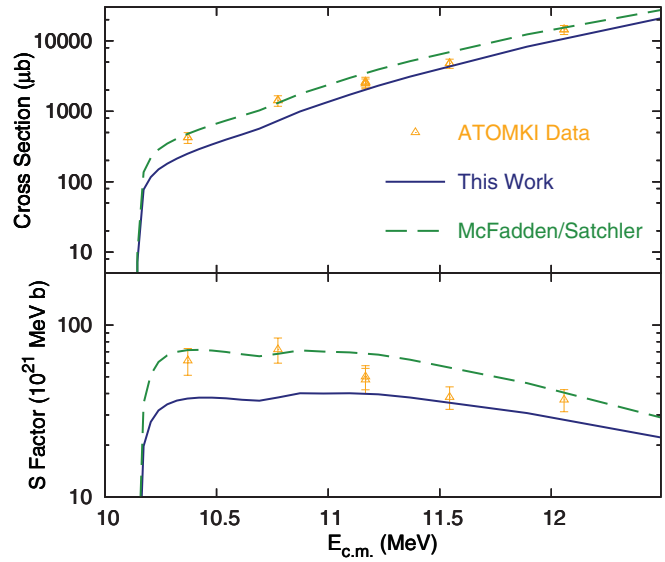

FIG. 17. (Color online) Cross sections and S factors of ^{106}Cd(α,n). Experimental data points were taken from Ref. [12]. The solid line was calculated using the new parametrization for the α-optical potential while the McFadden and Satchler potential [29] was used for the dashed line.

V. HF CALCULATIONS FOR (α,x) REACTIONS

The cross sections of the α-induced reactions were calculated with the HF computer code CIGAR [45]. CIGAR represents a modified version of the classical code SMOKER [46] with substantial optimization in terms of the description of the energy dependence of the level density [47] as well as an improved treatment of the Coulomb wave functions [45]. The code was adapted to accommodate various potential parametrizations for easy comparison. In particular, the new parametrization described in the previous section was adopted for the α-optical potential. The widely used global model of McFadden and Satchler [29] and the global potential of Demetriou *et al.* (Potential I) [34] were also used for comparison. The γ-transmission coefficient was calculated using the approach described in Ref. [48]. The nucleon (n or p) potential was taken from the global parametrization in Ref. [49]. The level density was calculated using the back-shifted Fermi gas formalism with the astrophysics-oriented parametrization from Ref. [50].

To compare the calculations with data, activation experiments done in the past were reviewed. In particular, we considered the measurements of (α,x) cross sections on Te, Sn, and Cd isotopes: ^{120}Te(α,n) measured at ND [51]; ^{106}Cd(α,$\gamma/p/n$) measured at ND and ATOMKI [12]; ^{112}Sn(α,γ/p) measured at ND [13]; ^{118}Sn(α,n) measured in Romania [14]. In the last one, a measurement of ^{117}Sn(α,γ) cross sections was claimed and we shall demonstrate later that it came most likely from the ^{118}Sn(α,n) reaction due to the impurity of the targets.

Figures 16–18 show the cross sections and S factors of the α-induced reactions on ^{106}Cd. The data were taken from Ref. [12] and compared with the calculations using the new parametrization proposed in Sec. IV B (solid lines), that of McFadden and Satchler [29] (dashed lines), and Potential I of Demetriou *et al.* [34] (dotted lines) for the α-optical potential. As shown in the plots, the agreement between data and calculations for the (α,n/p) cross sections is generally good to within a factor of two. The small deviations probably come from uncertainties associated with the global nucleon potential model or level density. However,

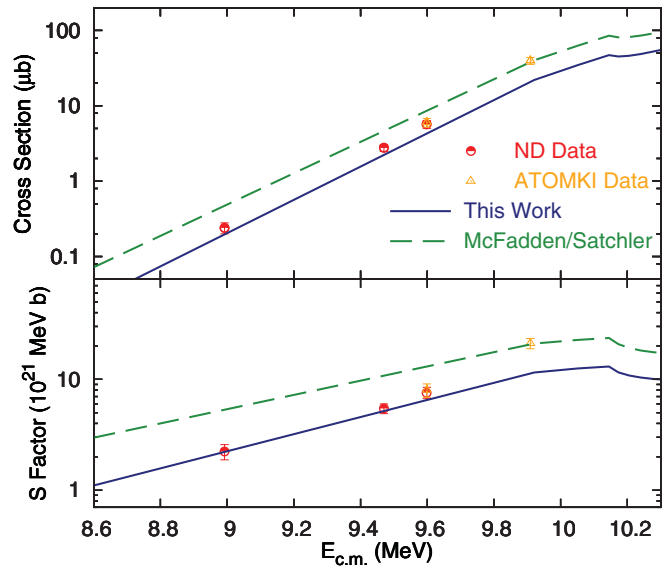

FIG. 18. (Color online) Cross sections and S factors of ^{106}Cd(α,p). Experimental data points were taken from Ref. [12]. The solid line was calculated using the new parametrization for the α-optical potential while the McFadden and Satchler potential [29] was used for the dashed line.

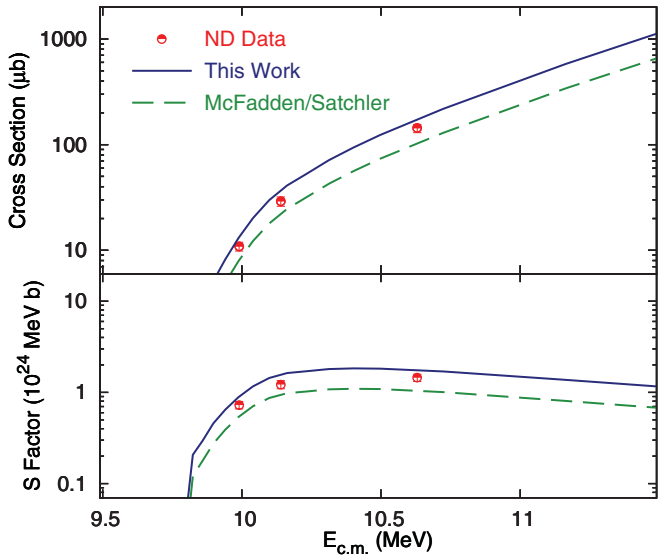

FIG. 19. (Color online) Cross sections and S factors of ^{120}Te(α,n). Experimental data points were from Ref. [51]. The solid line was calculated using the new parametrization for the α-optical potential while the McFadden and Satchler potential [29] was used for the dashed line.

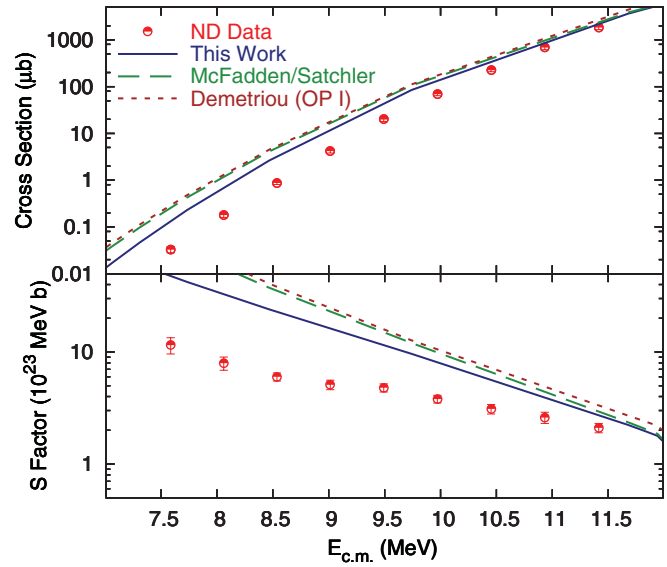

FIG. 20. (Color online) Cross sections and S factors of ^{112}Sn(α,γ). Experimental data points were taken from Ref. [13]. The solid line was calculated using the new parametrization for the α-optical potential while the calculations from the McFadden and Satchler potential [29] (dashed lines) and the potential of Demetriou *et al.* (Potential I) [34] (dotted lines) were also shown for comparisons.

the calculations are systematically higher than the data for the (α,γ) reaction cross sections even though the calculation with the new α-potential parametrization shows improved agreement. The discrepancies diminish toward higher energies while becoming significantly larger at lower energies. Such an effect seems to be related to the radiative capture channel only. However, note that the (α,γ) reaction data extend to a much lower energy range than the (α,n/p) reactions due to the Q-value differences. It may be the reason why the effect is not seen in the n/p channels. Therefore it is still possible that an unexpected low energy effect was not properly formulated in the parametrization of the α-optical potential.

The cross sections and S factors of ^{120}Te(α,n) reaction are shown in Fig. 19. The data are taken from recent experimental work at Notre Dame [51] and the calculations are also shown for the new parametrization (solid line) and that of McFadden and Satchler [29] (dashed line) for the α-optical potential, respectively. The calculations agree with the data to within 40%. The difference is probably again due to the uncertainty of the global nucleon potential model.

Figures 20 and 21 show the case for ^{112}Sn(α,γ/p) reactions. The data were taken from Ref. [13]. For the (α,p) reaction, the calculations match the data very well. However, similar discrepancies occur for the case of ^{112}Sn(α,γ) as in the case of ^{106}Cd(α,γ). The new parametrization provided a better calculation but the systematic overprediction of the cross sections, in particular at the low energy end [lower than that for the (α,p) reaction], suggests again that better treatment of the γ strength and/or the α-optical potential is needed at very low energies. Further discussion of the effect is elaborated on in the next section.

A measurement of ^{117}Sn(α,γ) cross sections was claimed in Ref. [14]. As shown in Fig. 22, the calculations (two dotted and dot-dashed curves at bottom) corresponding to this reaction were compared to the data. The large underestimate, especially at the two higher energy points, exceeding an order of magnitude, does not follow the trend of overprediction for other (α,γ) reactions discussed above. In fact we will show that the observed cross sections were most likely from the (α,n) reaction on ^{118}Sn resulting from target impurities.

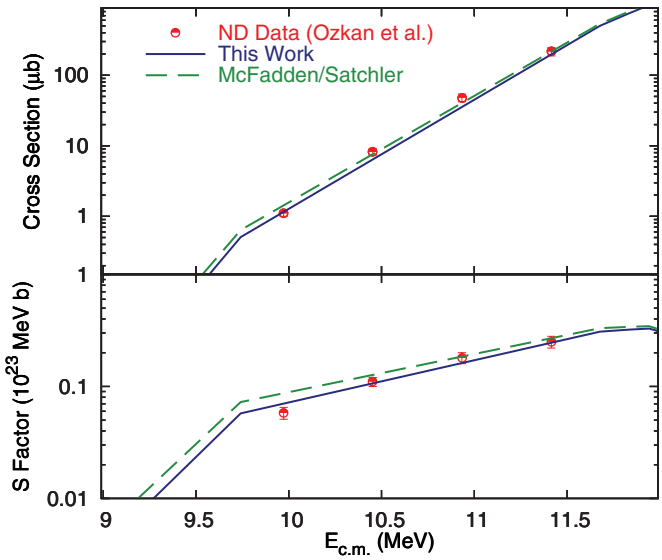

FIG. 21. (Color online) Cross sections and S factors of ^{112}Sn(α,p). Experimental data points were taken from Ref. [13]. The solid line was calculated using the new parametrization for the α-optical potential while the McFadden and Satchler potential [29] was used for the dashed line.

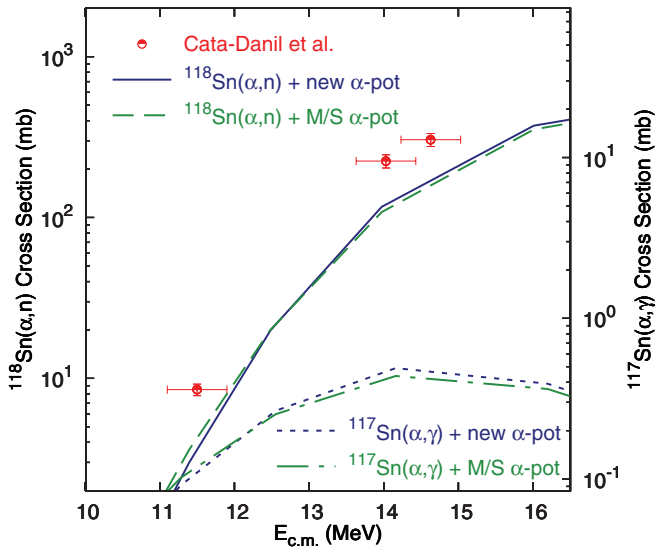

FIG. 22. (Color online) Cross sections of ^{118}Sn(α,n) reaction. Experimental data points were taken from Ref. [14]. The solid line was calculated using the new parametrization for the α-optical potential while the McFadden and Satchler potential [29] was used for the dashed line. The dotted and dot-dashed lines were calculated for the ^{117}Sn(α,γ) reaction as assumed in Ref. [14].

According to Ref. [14], the targets consist of 90% ^{117}Sn and 3.81% ^{118}Sn. Since ^{118}Sn(α,n) reaction produces the same final product of ^{121}Te as ^{117}Sn(α,γ), the claimed ^{117}Sn(α,γ) cross sections from counting the γ decays of ^{121}Te can then be converted to that of ^{118}Sn(α,n) assuming that all the decays were from ^{118}Sn(α,n) instead of ^{117}Sn(α,γ). The converted cross sections can be read from the scale of the left vertical axis in Fig. 22. In light of the thickness of the targets ($\sim$4.5 mg/cm^2) [14], we put error bars of $\pm$0.4 MeV on the data points to depict the range of the beam energy loss in targets. The calculations corresponding to ^{118}Sn(α,n) (solid and dashed lines) agree much better with the converted data. The agreement would be even better if we consider that the data points should be more representative at energies corresponding to the right end of the error bars owing to the thickness of the targets.

VI. ASTROPHYSICAL IMPLICATIONS AND CONCLUSIONS

We have systematically studied the α elastic scattering on Te, Sn, and Cd isotopes. A new energy and mass dependent parametrization of the α-optical potential derived from the new experimental elastic cross sections is proposed. HF calculations with the new parametrization are compared to the existing activation data on (α,x) reactions. Reasonably good agreements on the (α,n/p) reactions were achieved considering the uncertainty of the global nucleon optical potential model used.

However, the new predictions for the (α,γ) reactions are still consistently higher than the data even though improvements are seen. The agreement is good at the high energy end but becomes progressively worse toward the low energy end. Unfortunately the cross sections at low energy are more relevant to the astrophysical rate, i.e., closer to the so-called Gamow peak. This energy-dependent systematic overestimation from the HF calculations for the (α,γ) reaction cross sections indicates that an unknown effect suppresses the cross sections at very low energies. It may be tied to the treatment of the gamma strength since no such effect is seen in other reaction channels. In particular, better estimation, for example, including pygmy resonances [52–54], may be necessary to solve the discrepancy. Detailed studies of the effect of the γ strength functions on photonuclear and radiative-capture reactions can be seen in the work of Beard *et al.* [54].

On the other hand, the disagreement for (α,γ) reactions occurs more dramatically at lower energies where (α,n/p) reactions cannot reach due to Q-value limitations. It may exist for all the possible reaction channels at low energies. Therefore mistreatment of the entrance channel especially on the α-optical potential cannot be excluded. More experimental studies on (α,n/p) reactions at lower energies ($<$10 MeV) will help clarify the issue.

Such an overestimation for (α,γ) could also possibly be resolved by introducing a small surface term at large radius in the imaginary part of the α-optical potential for inelastic scattering as proposed by Mohr [55]. Further studies, especially regarding the inelastic channel, are clearly needed to improve the HF predictions for the (α,γ) rates.

A different parametrization may be needed for the α-optical potential to account for the low energy anomaly. To reduce the sensitivity of the parameters to energy, other double-folding models [56,57] can be studied for better treatment of the energy dependence. For simplicity, we assumed a spherical shape for the potential parametrization. Future studies should include deformation in these heavy nuclei for better description.

More systematic experimental work is in need besides the aforementioned inelastic and (α,x) reactions. In particular, our measurements were limited by the range of $48 \leqslant Z \leqslant 52$. Future experiments with an extended Z range will help constrain the Z dependence of the α-optical potential parameters. In addition, similar studies for reactions in other mass ranges are needed in order to determine how the optical potential evolves on the nuclear chart. HF calculations for the (γ,α) rates related to the astrophysical p process will not be reliable without further investigation on this issue.

ACKNOWLEDGMENTS

We thank P. Mohr and D. Galaviz for helpful discussions. This work has been supported by the National Science Foundation under Grant No. PHY0758100 and the Joint Institute for Nuclear Astrophysics, NSF-PFC under Grants No. PHY0822648 and PHY0216783. Zs.F., G.G.K., and E.S. also gratefully acknowledge the support of OTKA NN83261 (EUROGENESIS), OTKA 101328 and European Research Council, Grant No. 203175. N.Ö., G.E., and R.T.G. have also been supported by TUBİTAK (Grants No. 104T2467 and 108T508).

[1] M. Arnould and S. Goriely, Phys. Rep. **384**, 1 (2003).
[2] S. E. Woosley and W. M. Howard, Astrophys. J. Suppl. Ser. **36**, 285 (1978).
[3] W. M. Howard, B. S. Meyer, and S. E. Woosley, Astrophys. J. Lett. **373**, L5 (1991).
[4] S.-i. Fujimoto, M.-a. Hashimoto, O. Koike, K. Arai, and R. Matsuba, Astrophys. J. **585**, 418 (2003).
[5] W. Rapp, J. Görres, M. Wiescher, H. Schatz, and F. Käppeler, Astrophys. J. **653**, 474 (2006).
[6] W. Hauser and H. Feshbach, Phys. Rev. **87**, 366 (1952).
[7] T. Rauscher, Phys. Rev. C **73**, 015804 (2006).
[8] C. Nair, A. R. Junghans, M. Erhard, D. Bemmerer, R. Beyer, E. Grosse, K. Kosev, M. Marta, G. Rusev, K. D. Schilling *et al.*, Phys. Rev. C **81**, 055806 (2010).
[9] Z. Fülöp, Á.Z. Kiss, E. Somorjai, C. Rolfs, H. Trautvetter, T. Rauscher, and H. Oberhummer, Z. Phys. A **355**, 203 (1996).
[10] E. Somorjai, Z. Fülöp, A. Z. Kiss, C. E. Rolfs, H. P. Trautvetter, U. Greife, M. Junker, S. Goriely, M. Arnould, M. Rayet *et al.*, Astron. Astrophys. **333**, 1112 (1998).
[11] W. Rapp, M. Heil, D. Hentschel, F. Käppeler, R. Reifarth, H. J. Brede, H. Klein, and T. Rauscher, Phys. Rev. C **66**, 015803 (2002).
[12] G. Gyürky, G. G. Kiss, Z. Elekes, Z. Fülöp, E. Somorjai, A. Palumbo, J. Görres, H. Y. Lee, W. Rapp, M. Wiescher *et al.*, Phys. Rev. C **74**, 025805 (2006).
[13] N. Özkan, G. Efe, R. T. Güray, A. Palumbo, J. Görres, H. Y. Lee, L. O. Lamm, W. Rapp, E. Stech, M. Wiescher *et al.*, Phys. Rev. C **75**, 025801 (2007).
[14] I. Căta-Danil, D. Filipescu, M. Ivaşcu, D. Bucurescu, N. V. Zamfir, T. Glodariu, L. Stroe, G. Căta-Danil, D. G. Ghiţă, C. Mihai *et al.*, Phys. Rev. C **78**, 035803 (2008).
[15] C. Yalçin, R. T. Güray, N. Özkan, S. Kutlu, G. Gyürky, J. Farkas, G. G. Kiss, Z. Fülöp, A. Simon, E. Somorjai *et al.*, Phys. Rev. C **79**, 065801 (2009).
[16] G. Gyürky, Z. Elekes, J. Farkas, Z. Fülöp, Z. Halász, G. G. Kiss, E. Somorjai, T. Szücs, R. T. Güray, N. Özkan *et al.*, J. Phys. G **37**, 115201 (2010).
[17] G. Kiss, T. Rauscher, T. Szücs, Z. Kertész, Z. Fülöp, G. Gyürky, C. Fröhlich, J. Farkas, Z. Elekes, and E. Somorjai, Phys. Lett. B **695**, 419 (2011).
[18] T. Rauscher and F. Thielemann, At. Data Nucl. Data Tables **79**, 47 (2001).
[19] P. Mohr, T. Rauscher, H. Oberhummer, Z. Máté, Z. Fülöp, E. Somorjai, M. Jaeger, and G. Staudt, Phys. Rev. C **55**, 1523 (1997).
[20] Z. Fülöp, G. Gyürky, Z. Máté, E. Somorjai, L. Zolnai, D. Galaviz, M. Babilon, P. Mohr, A. Zilges, T. Rauscher *et al.*, Phys. Rev. C **64**, 065805 (2001).
[21] D. Galaviz, Z. Fülöp, G. Gyürky, Z. Máté, P. Mohr, T. Rauscher, E. Somorjai, and A. Zilges, Phys. Rev. C **71**, 065802 (2005).
[22] G. G. Kiss, Z. Fülöp, G. Gyürky, Z. Máté, E. Somorjai, D. Galaviz, A. Kretschmer, K. Sonnabend, and A. Zilges, Eur. Phys. J. A **27**, 197 (2006).
[23] G. G. Kiss, P. Mohr, Z. Fülöp, D. Galaviz, G. Gyürky, Z. Elekes, E. Somorjai, A. Kretschmer, K. Sonnabend, A. Zilges *et al.*, Phys. Rev. C **80**, 045807 (2009).
[24] G. G. Kiss, P. Mohr, Z. Fülöp, G. Gyürky, Z. Elekes, J. Farkas, E. Somorjai, C. Yalcin, D. Galaviz, R. T. Güray *et al.*, Phys. Rev. C **83**, 065807 (2011).
[25] P. Tischhauser, A. Couture, R. Detwiler, J. Görres, C. Ugalde, E. Stech, M. Wiescher, M. Heil, F. Käppeler, R. E. Azuma *et al.*, Phys. Rev. C **79**, 055803 (2009).
[26] J. P. Greene and G. E. Thomas, Nucl. Instrum. Methods Phys. Res. A **282**, 71 (1989).
[27] J. P. Greene, A. Palumbo, W. Tan, J. Görres, and M. C. Wiescher, Nucl. Instrum. Methods Phys. Res. A **590**, 76 (2008).
[28] Micromatter, 4004 Wesbrook Mall, Vancouver, BC V6T 2A3, Canada.
[29] L. McFadden and G. R. Satchler, Nucl. Phys. **84**, 177 (1966).
[30] M. Avrigeanu, W. von Oertzen, A. J. M. Plompen, and V. Avrigeanu, Nucl. Phys. A **723**, 104 (2003).
[31] C. Fröhlich, diploma thesis, University of Basel, Basel, Switzerland (2002).
[32] T. Rauscher, Nucl. Phys. A **725**, 295 (2003).
[33] T. Rauscher, Nucl. Phys. A **719**, C73 (2003).
[34] P. Demetriou, C. Grama, and S. Goriely, Nucl. Phys. A **707**, 253 (2002).
[35] A. M. Kobos, B. A. Brown, P. E. Hodgson, G. R. Satchler, and A. Budzanowski, Nucl. Phys. A **384**, 65 (1982).
[36] A. Kobos, B. Brown, R. Lindsay, and G. Satchler, Nucl. Phys. A **425**, 205 (1984).
[37] M. Farid and G. Satchler, Nucl. Phys. A **438**, 525(1985).
[38] H. De Vries, C. W. De Jager, and C. De Vries, At. Data Nucl. Data Tables **36**, 495 (1987).
[39] E. B. Shera, M. V. Hoehn, G. Fricke, and G. Mallot, Phys. Rev. C **39**, 195 (1989).
[40] G. Fricke, C. Bernhardt, K. Heilig, L. A. Schaller, L. Schellenberg, E. B. Shera, and C. W. Dejager, At. Data Nucl. Data Tables **60**, 177 (1995).
[41] H. Abele, A0 code, University of Tübingen.
[42] H. Abele and G. Staudt, Phys. Rev. C **47**, 742 (1993).
[43] F. James and M. Roos, Comput. Phys. Commun. **10**, 343 (1975), URL [http://seal.web.cern.ch/seal/work-packages/mathlibs/minuit/home.html].
[44] U. Atzrott, P. Mohr, H. Abele, C. Hillenmayer, and G. Staudt, Phys. Rev. C **53**, 1336 (1996).
[45] R. Crowter, Master's thesis, University of Surrey, UK, 2007.
[46] F. Thielemann, J. W. Truran, and M. Arnould, *Proceedings of the 2nd IAP Workshop on Advances in Nuclear Astrophysics* (Editions Frontieres, Paris, France, 1986), pp. 525–540.
[47] A. V. Ignatyuk, K. K. Istekov, and G. N. Smirenkin, Sov. J. Nucl. Phys. **29**, 450 (1979).
[48] F. Thielemann and M. Arnould, in *Proceedings of the International Conference on Nuclear Data for Science and Technology*, edited by K. H. Böckhoff (D. Reidel, Antwerp, Belgium, 1983), pp. 762–765.
[49] A. J. Koning and J. P. Delaroche, Nucl. Phys. A **713**, 231 (2003).
[50] T. Rauscher, F. K. Thielemann, and K. L. Kratz, Phys. Rev. C **56**, 1613 (1997).
[51] A. Palumbo, W. P. Tan, J. Görres, M. Wiescher, N. Özkan, R. T. Güray, and C. Yalçin, Phys. Rev. C **85**, 028801 (2012).
[52] N. Paar, D. Vretenar, E. Khan, and G. Colò, Rep. Prog. Phys. **70**, 691 (2007).
[53] E. G. Lanza, F. Catara, D. Gambacurta, M. V. Andrés, and P. Chomaz, Phys. Rev. C **79**, 054615 (2009).
[54] M. Beard, S. Frauendorf, B. Kämpfer, R. Schwengner, and M. Wiescher (submitted for publication).
[55] P. Mohr, *Book of Abstracts of p-Process Workshop* (Kocaeli University, Turkey, 2011), p. 21.
[56] D. T. Khoa, G. R. Satchler, and W. von Oertzen, Phys. Rev. C **56**, 954 (1997).
[57] E. Bauge, J. P. Delaroche, and M. Girod, Phys. Rev. C **58**, 1118 (1998).